Composite Structures 381 (2026) 120051



Contents lists available at ScienceDirect

Composite Structures

journal homepage: www.elsevier.com/locate/compstruct





Bond behavior between surface-treated 3D-printed FRP bars and concrete

Zi-Tong Yan [a,c], Xianwen Hu [a], Jie-Kai Zhou [a], Yan Zhuge [b], Jun-Jie Zeng [b,*]

[a] Department of Civil and Transportation Engineering, Guangdong University of Technology, Guangzhou 510006, China
[b] UniSA STEM, University of South Australia, South Australia 5095 Australia
[c] School of Future Transportation, Guangzhou Maritime University, Guangzhou 510006, China

ARTICLE INFO

Keywords:
3D printing
Pull-out test
Bond performance
Fused filament fabrication (FFF)
Continuous carbon fiber (CCF)
3D-printed fiber reinforced polymers (3DP-FRP) bar

ABSTRACT

Fiber-reinforced polymer (FRP) bars have been widely adopted as internal reinforcement for concrete structures, however, the conventional pultrusion fabrication process imposes limitations including reliance on molds and material waste. To address these issues, an innovative form of 3D-printed FRP (3DP-FRP) reinforcing bars based on additive manufacturing has recently been developed by the authors. In this study, a novel surface treatment for 3DP-FRP bars using serrated cross-section and sand coating is developed to enhance the bar-concrete interfacial bond performance. A total of 33 pull-out tests were performed to systematically investigate the effects of surface treatment methods, concrete strength, anchorage length, and bar diameter on the bond behavior of 3DP-FRP bars in concrete. Results show that untreated 3DP-FRP bars achieve a bond strength (the maximum average shear stress along the bonded length) of up to 7.3 MPa, markedly exceeding that of smooth pultruded bars. The bond strength increases with concrete strength but decreases with a greater anchorage length or bar diameter. The bars with a helical wrap and coarse sand coating (HWCS) exhibit the highest bond strength. Furthermore, the applicability of the modified BPE (mBPE) model for bond-slip characterization of 3DP-FRP bars is validated, and a new predictive equation for bond strength estimation is proposed.

1. Introduction

Additive Manufacturing (AM), known as 3D printing and as opposed to subtractive manufacturing methodologies, is an advanced technology that manufactures components based on digital models. Major AM methods include Fused Filament Fabrication (FFF), Selective Laser Sintering (SLS), Stereolithography (SLA), and Laminated Object Manufacturing (LOM) [1–4]. Among these, FFF enables a mold-free fabrication of fiber-reinforced polymer (FRP) composites through layer-by-layer deposition and has been extensively applied in aerospace, automotive, biomedical, and sports equipment industries [5–10]. Notably, this technology enables on-site fabrication in concrete engineering [11,12], allowing the direct printing of FRP composites on structures for rapid reinforcement. 3D-printed FRP (3DP-FRP) can also be combined with 3D-printed concrete to form integrated composite structures which exhibit potential for Off-Earth construction [13]. The printing technology demonstrates environmental sustainability, characterized by the elimination of mold waste and the recyclability of materials [14,15].

Several studies have investigated the application of 3DP-FRP reinforcement in concrete structures. Zeng et al. [13] fabricated 3DP-FRP bars with hooked ends to enhance anchorage in UHPC, demonstrating that their employed significantly improves the mechanical performance of UHPC slabs. Additionally, Zeng et al. [12] employed 3DP-FRP stirrups with aligned carbon fiber filaments in the bent sections to confine concrete columns, which resulted in improved compressive strength. These findings highlight that the interfacial bond behavior between FRP bars and concrete plays a decisive role in stress transfer efficiency and overall load-bearing capacity. To address the application of 3DP-FRP bars, Yan et al. [11] developed specimens with a serrated surface texture, demonstrating the potential to significantly enhance bond performance with concrete. While the bond mechanisms of conventional FRP bars have been extensively studied [16–22], those of 3DP-FRP bars with serrated surfaces remain largely unexplored.

FRP reinforcement has been widely adopted in reinforced concrete structures [23,24], and substantial progress has been achieved in understanding the interfacial bond behavior between conventional FRP bars and concrete, revealing the effects of surface treatment, concrete strength, anchorage length, and bar diameter on bond performance [25,26]. These studies have been adopted to establish various predictive

* Corresponding author.
E-mail address: junjie.zeng@adelaide.edu.au (J.-J. Zeng).

https://doi.org/10.1016/j.compstruct.2026.120051
Received 13 August 2025; Received in revised form 23 December 2025; Accepted 7 January 2026
Available online 8 January 2026
0263-8223/© 2026 The Author(s). Published by Elsevier Ltd. This is an open access article under the CC BY license (http://creativecommons.org/licenses/by/4.0/).

Table 1
Parameters of CCF and PETG.

Component	Diameter (mm)	Tensile strength (MPa)	Density
CCF [46]	0.33	2300	145(Tex)
PETG [47]	1.75	34.77	1.27 (g/cm^3)

Note: The diameter and tensile strength of the CCF were measured in this study, while the other parameters were provided by the manufacturer.

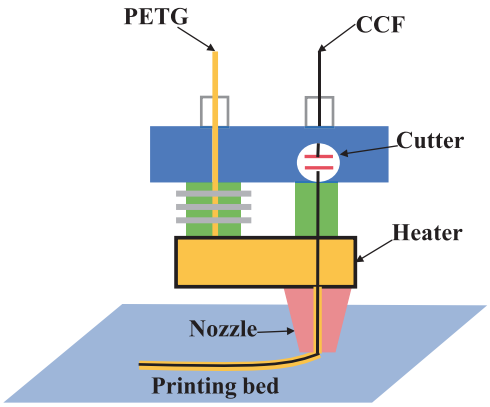


Fig. 1. The printing nozzle.

models for bond strength and bond–slip relationships [27–30]. Among the influencing parameters, the surface treatment of FRP bars is particularly critical [31–33] and has been explicitly addressed in the current design codes in determining bond behavior at the FRP–concrete interface. For instance, ACI 440.1R-15 [34] affirms that the surface texture of FRP bars significantly determines their bonding mechanism with concrete. In addition, CSA S806-12 [35] and CSA S6-14 [36] adopt different coefficients in the anchorage length equations for FRP bars with different surface treatment approaches.

Common surface treatments for FRP bars include sand-coated, ribbed (e.g., helically wrapped), and hybrid combinations [31–33]. Research [37–40] has demonstrated that coarse sand-coated FRP bars exhibit superior bond strength compared to fine sand-coated specimens. Notably, natural lake sands, due to their unique particle size distribution and surface morphology, provide better interfacial bonding than mechanically crushed sands [37]. The interfacial bond performance of ribbed FRP bars is significantly influenced by the rib geometric parameters, including helical angle, rib spacing, rib width, and rib height [40–42]. Deep-rib bars exhibit superior bond strength compared to shallow-rib specimens, while increased rib width and spacing were found to reduce bond strength. Additionally, studies demonstrate that hybrid sand-coating and ribbing treatments significantly enhance the interfacial bond performance of FRP bars in concrete, leading to their widespread engineering application [43–45]. Despite these advances, the bond performance of FRP bars still varies significantly due to differences in bar type, concrete composition, manufacturing process, and treatment method. Therefore, a systematic investigation of the bond mechanisms between 3DP-FRP bars with various surface treatments and concrete is essential to establish theoretical tools for bond performance evaluation.

To this end, this study presents experimental and analytical investigations on the bond behavior between 3DP-FRP bars and concrete. The bond strengths of untreated and surface-treated 3DP-FRP bars are obtained based on pull-out tests, and compare to conventional pultruded smooth FRP bars. Four surface treatment methods are applied to 3DP-FRP bars: (1) helically wrapped, (2) coarse sand-coated, (3) fine sand-coated, and (4) a hybrid treatment combining helical wrapping with coarse sand coating. Key parameters affecting the bond performance are systematically evaluated, including concrete strength, bar diameter, anchorage length, and surface treatments. The experimental results reveal the relationship between interfacial bonding mechanisms and surface conditions of 3DP-FRP bars under different treatment methods. Experimental bond-slip curves confirm the applicability of the mBPE model for 3DP-FRP bars. A predictive model for 3DP-FRP bar bond strength is developed, providing theoretical support for engineering applications.

2. Materials and experimental procedures

2.1. Raw materials and printing process design of 3DP-FRP bars

The 3DP-FRP bars consist of continuous carbon fiber (CCF) filaments and thermoplastic polyethylene terephthalate glycol-modified (PETG) filament. The CCF filament has a fiber volume fraction of 60%, achieved through vacuum-assisted epoxy resin impregnation and an elastic modulus of 145 GPa. Each CCF filament has a diameter of 0.33 mm and consists of 1500 carbon fibers. The PETG filament has a diameter of 1.75 mm and a density of 1.27 g/cm^3. This PETG filament serves as the co-extrusion material, extruded together with CCF. The detailed parameters of both materials are presented in Table 1.

The co-extrusion printing nozzle design is illustrated in Fig. 1, featuring separate inlets for CCF and molten PETG. 3DP-FRP bars were fabricated with diameters of 3, 4, and 5 mm using NanoCAD for geometric modeling and G-code generation. The distribution of CCF filaments in 3DP-FRP bars is shown in Fig. 2. The layer thickness was set to 0.33 mm, with a fixed fiber volume fraction of 32.6%. During the printing process, the printing speed was maintained at 300 mm/min. The printing nozzle and printing bed temperatures were kept at 240°C and 80°C, respectively. The parameters in Table 2 are defined as: D for diameter in mm, and f_v% for the fiber volume fraction in percentage.

2.2. Material properties of pultruded and 3DP-FRP bars

According to ASTM D7205/D7205M-21 [48], tension tests were conducted on 3DP-FRP bars with diameters of 3 mm, 4 mm, and 5 mm, as well as on pultruded CFRP bars [47,49] with a diameter of 4 mm and a 70% fiber content. Three replicates were tested for each configuration. The tensile strength, elastic modulus, and other material properties of the bars based on three samples are summarized in Table 3. The specimen ID is defined as follows: “P” denotes the 3DP-FRP bar, “T” denotes the pultruded bar, and “D” denotes the nominal diameter. As shown in Table 3, the elastic modulus of specimen P-D4 is 71.5 GPa, significantly lower than the 120.8 GPa of specimen T-D4. This difference is primarily due to their distinct fiber volume fractions, with the 3DP-FRP bar and the pultruded bar having values of 32.6% and 70%, respectively.

2.3. Surface treatment of 3DP-FRP bars

Fig. 3 compares the cross-sectional and longitudinal morphology of pultruded and 3DP-FRP bars. The pultruded CFRP bars exhibit smooth surfaces, whereas the 3DP-FRP bars display distinct serrated surface textures (Figs. 3b, 3d, and 3f). For the 3DP-FRP bars, four surface treatment methods were employed: helically wrapping (HW), coarse sandblasting (CS), fine sandblasting (FS), and combined coarse sandblasting with helical wrapping (HWCS). Fig. 4 illustrates the quartz sand blasting process on the 3DP-FRP bar surface. The quartz sand was classified into two distinct groups with particle sizes of 0.5–0.7 mm for the coarse group and 0.2–0.4 mm for the fine group. Epoxy resin served as the bonding agent to fully impregnate the quartz sand. The impregnated sand was then coated onto the FRP bar surface and cured at ambient temperature for 24 h. The surface morphologies of 3DP-FRP bars bonded with coarse and fine quartz sand are shown in Fig. 5(a) and Fig. 5(b).

Fig. 6 demonstrates the process of PET strand wrapping on 3DP-FRP

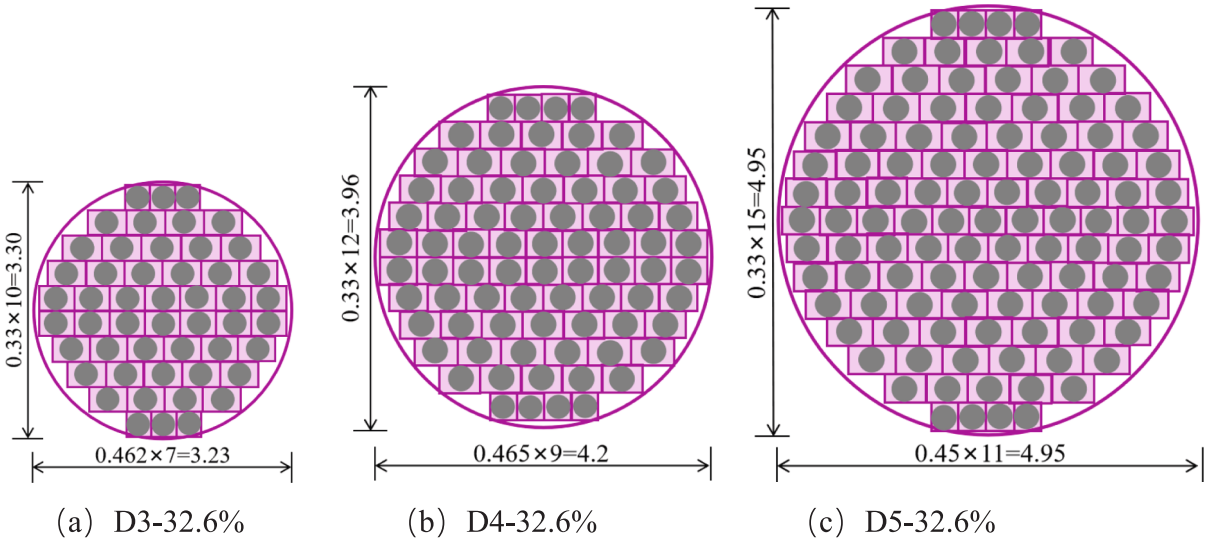


Fig. 2. The distribution of CCF filaments in 3DP-FRP bars. (unit: mm).

Table 2
Specimen parameters of 3DP-FRP bars.

Specimen	L (mm)	*Fiber* volume fraction (%)	Cross-section (mm^2)	*Fiber* count
D3-32.6%	0.33	32.6	7.89	50
D4-32.6%	0.33	32.6	12.40	78
D5-32.6%	0.33	32.6	17.28	109

Note: L—layer thickness; D—diameter of the 3DP-FRP bar; f_v—fiber volume fraction (%).

bars. The PET strands [50] had a diameter of 0.7 mm, with each strand consisting of 850 fibers and exhibiting a tensile strength of 600 MPa. Prior to performing the PET strand wrapping process, precise positioning lines were marked on the 3DP-FRP bar surface to determine the rib spacing and helical angle. Initially, untwisted PET fibers were gathered into strands using a rotating machine, then impregnated with epoxy resin. The strands were precisely wrapped onto the 3DP-FRP bar surface following the positioning lines, with subsequent 24-hour curing at ambient temperature. The HW FRP bar featured a rib height (h) of 1 mm, rib width (w) of 1.5 mm, dent width of 4 mm, rib spacing of 5.5 mm, and a winding angle of 55°, as shown in Fig. 5(c). The HWCS 3DP-FRP bars combined a hybrid of coarse sandblasting and helical wrapping surface treatments, as shown in Fig. 5(d).

The effective diameters of 3DP-FRP bars with different surface treatments were measured by immersing a prescribed length of the bars in water in accordance with ASTM D7205/D7205M-21 [48]. For 3DP-FRP bars with a nominal diameter of 3.97 mm, the effective diameters were 4.50 mm for fine sand-coated (FS), 4.70 mm for coarse sand-coated (CS), 4.44 mm for helically wrapped (HW), and 5.20 mm for helically wrapped and coarse sand-coated (HWCS) specimens. The HWCS specimens with nominal diameters of 3 mm and 5 mm measured effective diameters of 4.20 mm and 6.20 mm, respectively. The effective diameters of all FRP bars are summarized in Table 6, while the surface morphologies of all specimens are shown in Fig. 7.

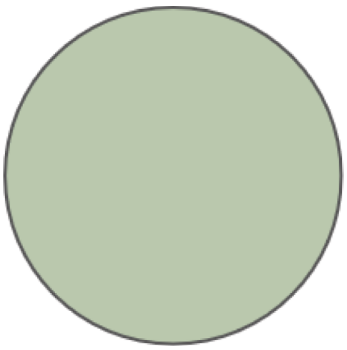
2.4. FRP-concrete specimen

To investigate the influence of concrete strength on the bond behavior with FRP bars, C50 and C80 concrete mixtures were prepared for this study. The C50 concrete mixture, designed for a targeted compressive strength of 55 MPa, consisted of cement of PO 42.5R, 5–10 mm crushed gravel (CG), and river sand (RS) with a maximum particle size of 2.36 mm. The C50 mix proportions are detailed in Table 4. The C80 concrete was fabricated using cement of PO 42.5R, fly ash (FA), CG with 5–10 mm, RS with a particle size of less than 1.18 mm, and a polycarboxylate superplasticizer (SP). Table 5 lists the proportions of the C80 mixture.

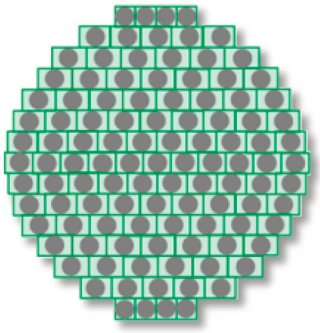
This study employed eleven distinct FRP-concrete pull-out specimen

Table 3
Material performance parameters of pultruded and 3DP-FRP bars.

Specimen ID	Diameter (mm)	Cross-sectional area (mm^2)	Tensile strength (MPa)	Tensile strength		Elastic modulus (GPa)	Elastic modulus	
				Average (MPa)	COV (%)		Average	COV(%)
P-D3-I	3	7.89	924.0		0.95	72.9		0.34
P-D3-II	3	7.89	932.8	932.8		73.2	73.2	
P-D3-III	3	7.89	941.7			73.4		
P-D4-I	4	12.40	908.1		1.72	72.4	71.5	1.14
P-D4-II	4	12.40	879.8	890.6		70.9		
P-D4-III	4	12.40	883.9			71.1		
P-D5-I	5	17.28	859.4		3.65	71.5		2.13
P-D5-II	5	17.28	799.5	827.3		71.3	70.5	
P-D5-III	5	17.28	822.9			68.8		
T-D4-I	4	12.57	1817.5	1742.5	3.84	121.2	120.8	0.63
T-D4-II	4	12.57	1721.3			121.4		
T-D4-III	4	12.57	1688.6			120.0		



(a) Pultruded FRP bar (Design drawing) (Ratio: 10:1)



(b) 3DP-FRP bar (Design drawing) (Ratio: 10:1)



(c) Smooth surface of pultruded FRP bar (Ratio: 10:1)



(d) Serrated surface of 3DP-FRP bar (Ratio: 10:1)



(e) Pultruded FRP bar (Ratio: 2:1)



(f) 3DP-FRP bar (Ratio: 2:1)

Fig. 3. Cross-sectional and longitudinal views of pultruded FRP and 3DP-FRP bars.

types, with three repetitions per type. In total, 33 specimens were cast, and their parameters are detailed in Table 6. The bars were designated according to the following coding system: The first code, "P", denotes 3DP-FRP bars, while "T" refers to pultruded FRP bars; the second code "D" specifies the nominal diameter; the third code "nd" defines the anchorage length, where n represents multiples of the effective bar diameter; the fourth code indicates the surface treatment; and the final code designates the concrete strength (N for C50 and H for C80). Specimens P-D4-5d-N and T-D4-5d-N exclude the surface treatment code due to their untreated surface conditions.

The pull-out specimens were designed according to CSA S806-12 [35], as shown in Fig. 8. The concrete specimens were cubes (100 mm × 100 mm × 100 mm) with the bar centrally embedded. The bond length, l_b, was expressed as a multiple of the bar diameter, d (i.e., $l_b = nd$), with values of n = 3, 5, and 7 adopted in this study. Fig. 9 illustrates the fabrication process of mould-cast concrete specimens. FRP bars were inserted into pre-drilled holes in the mould, sealed in place with adhesive, and subsequently well-prepared concrete was poured into the mould. All specimens in Tables 4, 5, and 6 were cured for 28 days under standard conditions of 20 ± 2°C temperature and 95 ± 5% relative humidity before testing.

2.5. Test setup and instrumentation

Pull-out tests were performed on a DDL-300 universal testing machine (DDL-300) under displacement-controlled loading at a rate of 0.5 mm/min. As shown in Fig. 10, three Linear Variable Differential Transformers (LVDTs) were positioned to measure the slip of the 3DP-FRP bars. One LVDT (LVDT 1) was installed at the free end to measure the relative displacement between the 3DP-FRP bar and the concrete. Two additional LVDTs (LVDT 2 and LVDT 3) were installed at the loaded end to measure slip deformation at that location.

3. Test results and discussion

3.1. Failure modes

In this study, all specimens exhibited the expected pull-out failure

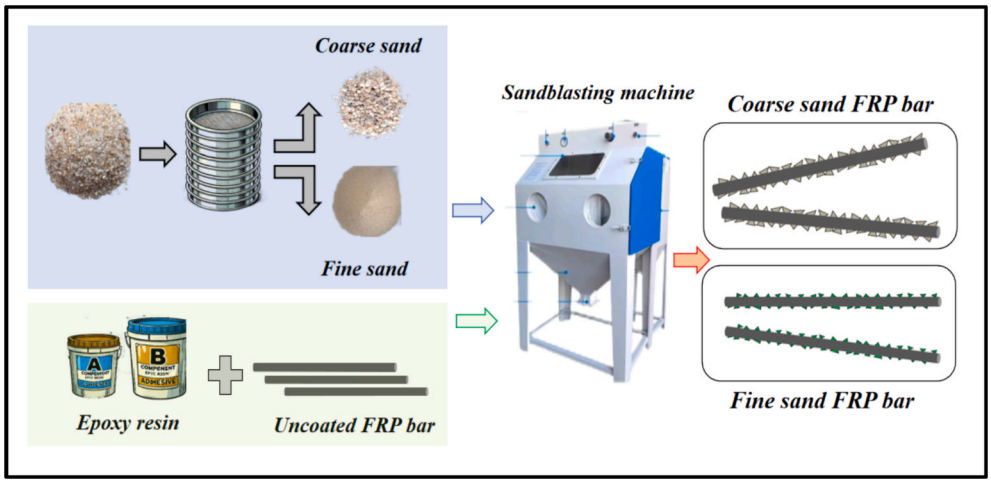


Fig. 4. Sand adhesion on 3DP-FRP.

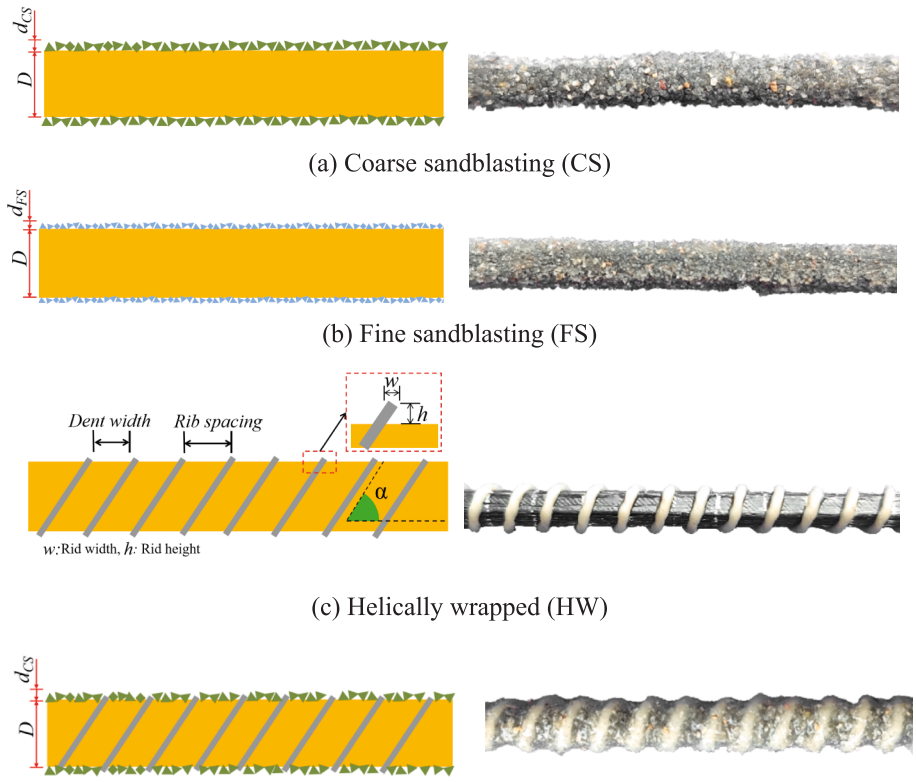


Fig. 5. Different surface treatments of 3DP-FRP bars.

mode. Significant slip was observed at the free end of the bars during testing. After testing, the concrete surface remained intact with no cracks observed, and the 3DP-FRP bars were not fractured. FRP bars were extracted from concrete for surface examination. The failure modes of all specimens are summarized in Fig. 11. As shown in Fig. 11(a), the fractured interface of pultruded FRP bars maintained a smooth surface without observable abrasion marks owing to their smooth surfaces. Consequently, the bars exhibited rapid slip and were completely pulled out, demonstrating no effective bonding. However, the untreated 3DP-FRP bars developed mechanical interlocking with concrete through their serrated cross-sections, resulting in significant surface abrasion with worn fiber residues adhering to the concrete interface (Fig. 11(b)). The white/grey areas shown in the right picture are concrete residue. The serrated cross-section of the 3DP-FRP bar caused concrete particles to be retained during the casting, curing, and pull-out processes. Fig. 11 (c) shows that the 3DP-FRP bar with HW surface maintained intact rib geometries with distinct indentations on the concrete surface. No interfacial shear wear or crushed concrete residues were observed between adjacent ribs. The interfacial region exhibited neither shear-induced wear nor fragmented concrete residues among the ribs. The sand-coated 3DP-FRP bars, as shown in Fig. 11(d), exhibited partial loss of both sand particles and resin matrix from their surfaces, which indicated insufficient adhesive bonding at the particle-FRP interface. In contrast, the HWCS 3DP-FRP bars exhibited significant resin residue

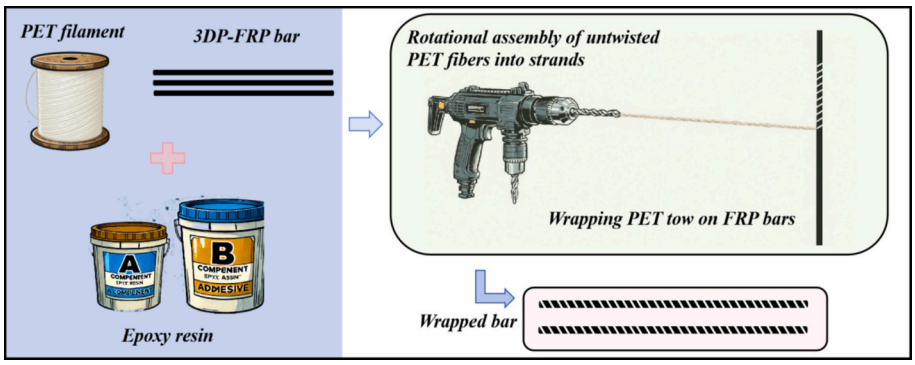


Fig. 6. PET strands wrapping on 3DP-FRP bars.

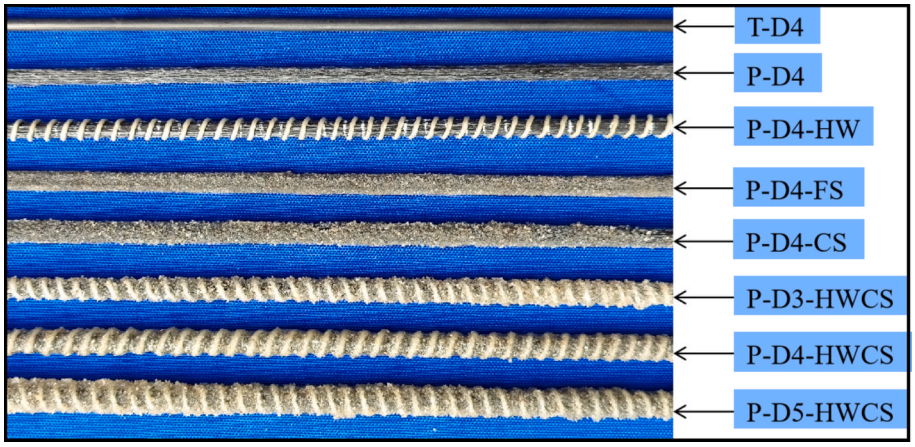


Fig. 7. Surface morphologies of all FRP bars in this study.

Table 4
Mix proportion of C50 (by weight).

PO 42.5R	RS	CG	Water	Average compressive strength (MPa)
1	2.03	3	0.6	55

Table 5
Mix proportion of C80 (by weight).

PO 42.5R	RS	CG	FA	SP	Water	Average compressive strength (MPa)
1	1.75	2.5	0.175	0.009	0.41	89

deposition at the concrete interface, as shown in Fig. 11(e) and 11(f). Localized surface material loss and rib abrasion damage were observed on the HWCS 3DP-FRP bars, suggesting a greater chemical bonding between the HWCS 3DP-FRP bars and concrete. Notably, the surface degradation of 3DP-FRP bars in C80 concrete was more severe than that in C50 concrete (see Fig. 11f).

3.2. Bond-slip behavior

Fig. 13 presents the average bond stress-slip curves (abbreviated as bond-slip curves in this study) of 3DP-FRP bar and concrete interfaces. In accordance with ACI 440.3R-12 [34], the actual slip is calculated by subtracting the deformation of the unbonded length (L_c) from the loaded-end displacement measured by a transducer, according to Equation (1) [26]. The bond stress between the concrete and the 3DP-FRP bars is defined as the average bond stress of the bonded area, which can be calculated according to Eq. (2).

Table 6
Parameter design of experimental specimens.

Specimen ID	Effective diameter (mm)	Anchorage length Multiples the diameter	Length (mm)	Concrete type	Production method
P-D3-5d-HWCS-N	4.20	5d	21.0	N	P
P-D4-3d-HWCS-N	5.20	3d	15.6	N	P
P-D4-5d-HWCS-N	5.20	5d	26.0	N	P
P-D4-7d-HWCS-N	5.20	7d	36.4	N	P
P-D5-5d-HWCS-N	6.20	5d	31.0	N	P
P-D4-5d-HW-N	4.44	5d	22.2	N	P
P-D4-5d-FS-N	4.50	5d	22.5	N	P
P-D4-5d-CS-N	4.70	5d	23.5	N	P
P-D4-5d-N	3.97	5d	19.9	N	P
P-D5-5d-HWCS-H	5.20	5d	26	H	P
T-D4-5d-N	4.00	5d	20	N	T

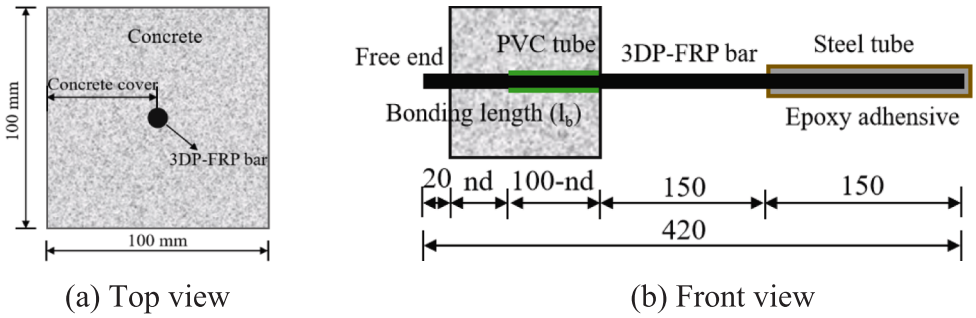


Fig. 8. FRP-concrete specimens for pull-out tests.

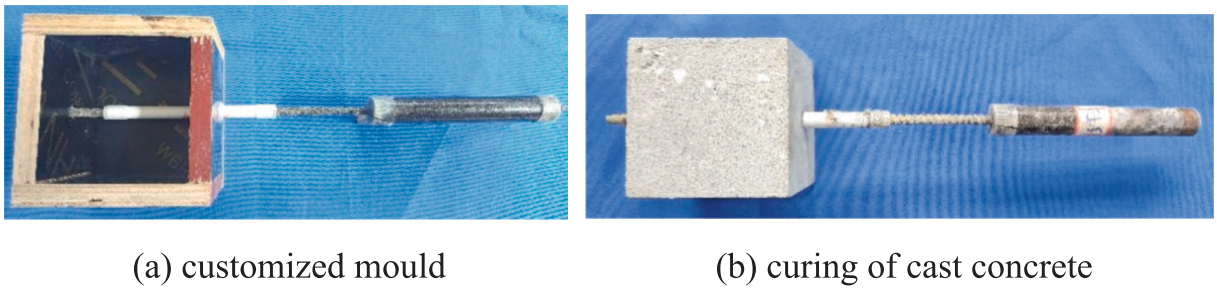


Fig. 9. Specimen preparation process.

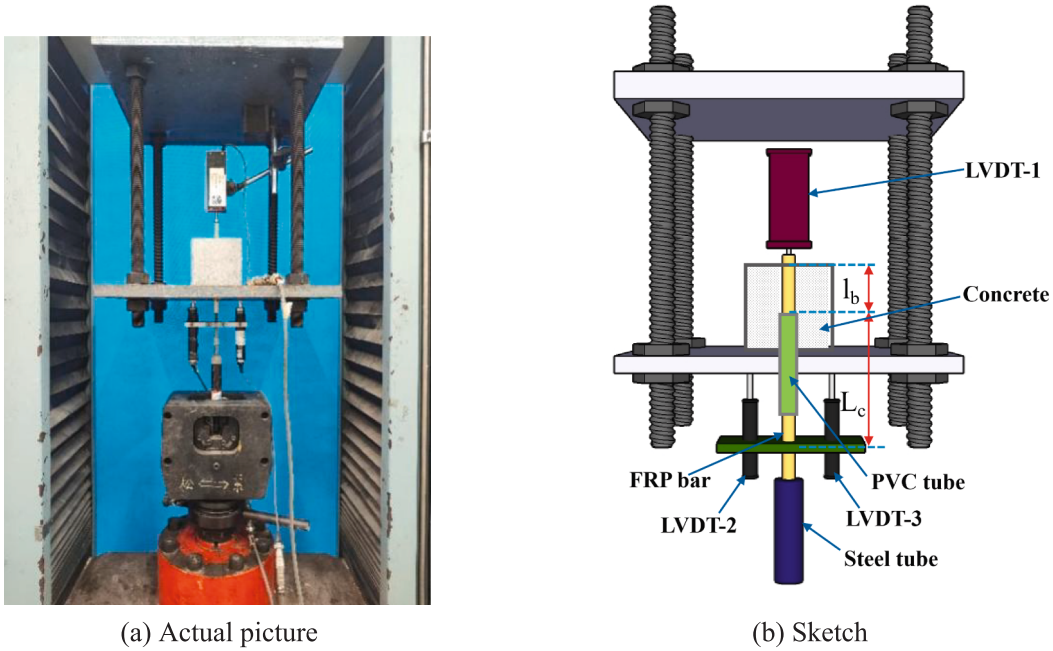


Fig. 10. Instrumentation and pull-out test setup.

$$S = S_l - \frac{PL_c}{E_l A_l} \quad (1)$$

$$\tau = \frac{P}{\pi d_b l_b} \quad (2)$$

where S_l is the displacement at the loading end; P is the peak load during loading process; L_c is the unbonded length near the loading end; E_l is the elastic modulus of FRP bar; A_l is the cross-section area of FRP bar calculated by the effective diameter d_b, and L_b is the anchorage length.

The maximum bond stress (τ_u) and the corresponding slip (s_u) values are listed in Table 7. Notably, due to the smooth surface of the conventional pultruded FRP bars, all three replicate specimens T-D4-5d-N exhibited negligible bond strength, confirming that the bonding was ineffective. Consequently, the corresponding data and curves are excluded from Table 7 and Fig. 13-14. The bond stress-slip curves for all specimen groups, as presented in Figs. 13(a)-13(d), exhibit four stages [51,52]. The bond behavior between FRP bars and concrete involves three primary mechanisms, which are chemical adhesion, frictional

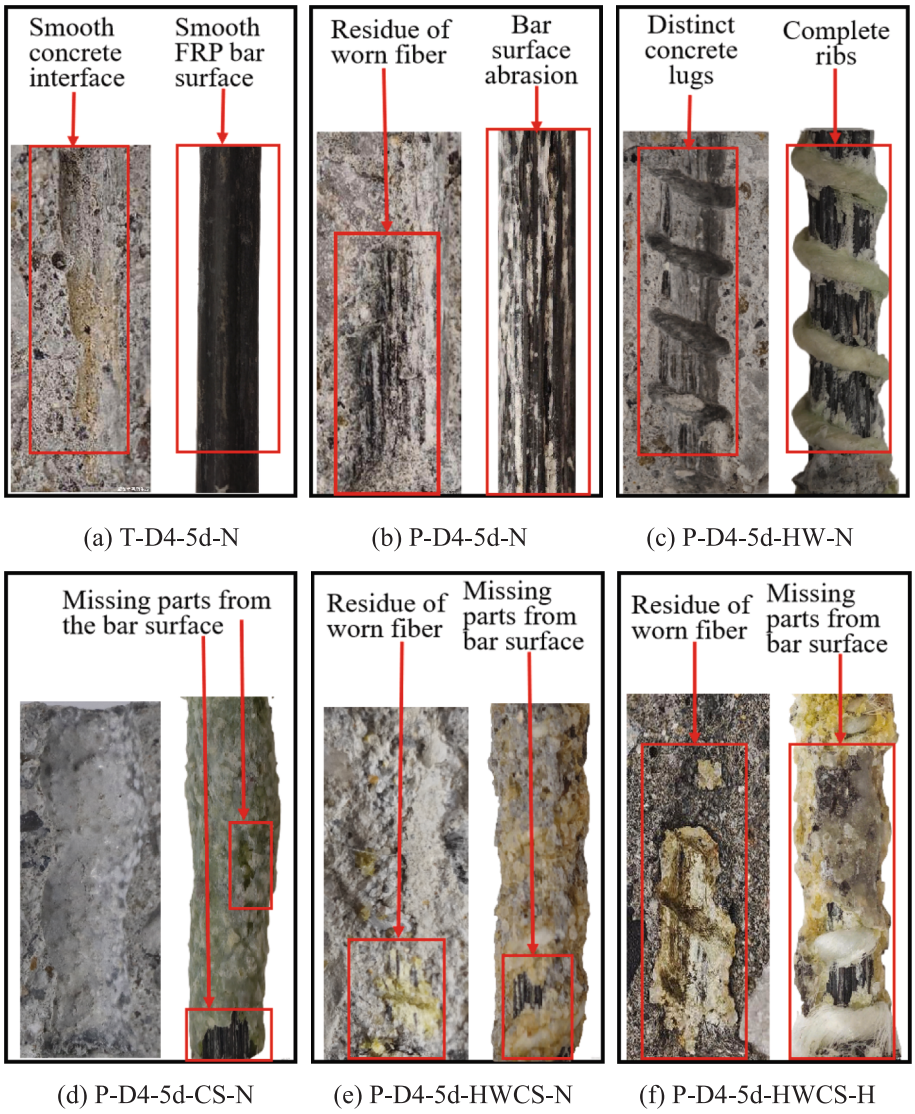


Fig. 11. Pull-out failure mode.

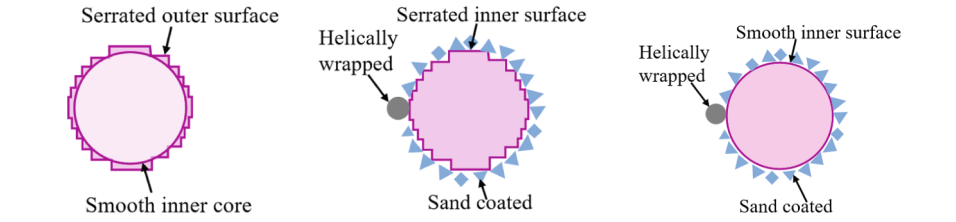


Fig. 12. The typical cross-sections of different FRP bars.

resistance, and mechanical interlock [51]. (1) In the first stage (i.e., elastic stage), the bond-slip curves exhibit steep slopes at small slip displacements, indicating high bond stiffness that primarily stems from chemical bonding (i.e., adhesive bonding) between the 3DP-FRP bars and cement hydration products at the interface. The bond-slip relationship exhibits fixed stiffness during this stage. (2) In the second stage (i.e., non-elastic stage), as loading increases, the interfacial bond stress develops mainly through frictional resistance and mechanical interlocking mechanisms, resulting in a gradual reduction of the bond-slip curve slope that approaches zero at the point of peak bond stress. (3) During the third stage (i.e., post-peak degradation stage), bond stress shows sustained reduction while slip displacement increases continuously, resulting from the gradual loss of mechanical interlocking resistance. (4) In the fourth stage (residual stage), the bond stress is primarily gained from the friction between the 3DP-FRP bar and concrete. As shown in Fig. 13(d), the bare 3DP-FRP bar in this study exhibits a typical descending trend due to the gradual wear of its surface serrations, which reduces friction over time (Fig. 12(a)). In contrast, Fig. 13(d)

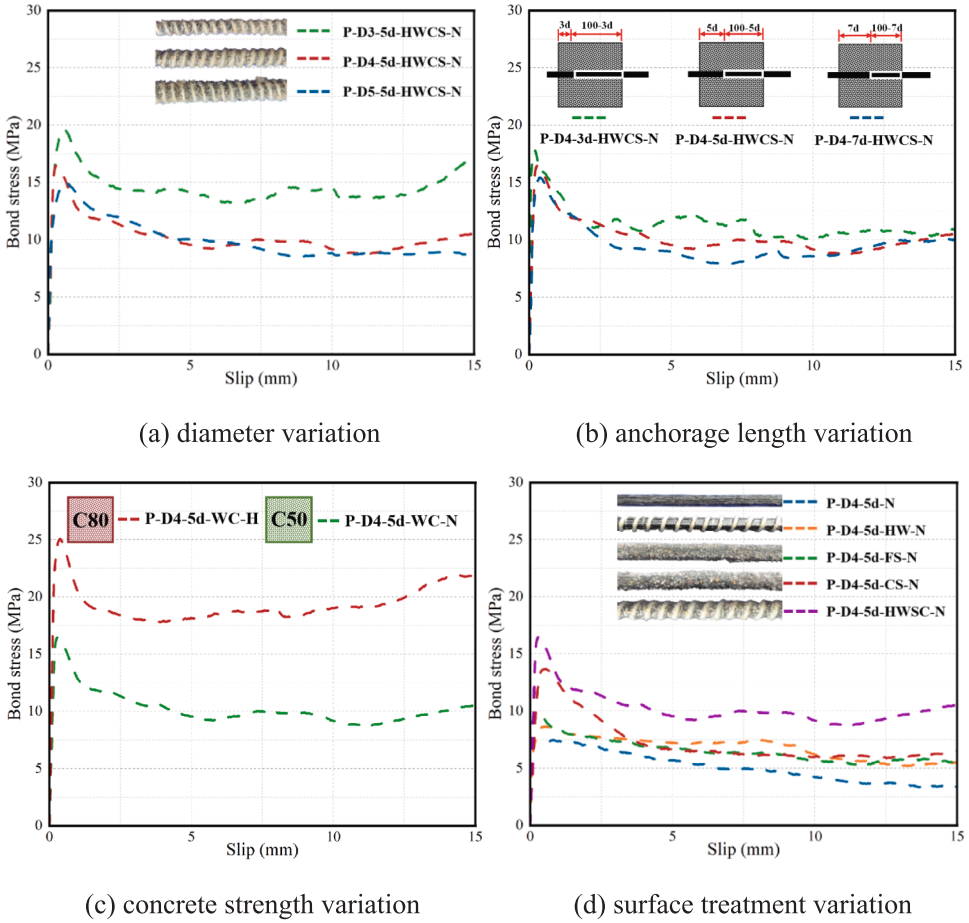


Fig. 13. Average bond stress–slip curves of pull-out specimens.

Table 7
Pull-out test results.

Specimen ID	τ_u(MPa)	Average	COV (%)	s_u(mm)	Average (mm)	COV (%)	Failure mode
P-D3-5d-HWCS-N	19.58	19.69	1.04	0.57	0.59	9.88	Pull-out
	19.93			0.66			
	19.57			0.55			
P-D4-3d-HWCS-N	17.78	18.69	4.82	0.21	0.21	4.76	Pull-out
	19.58			0.22			
	18.71			0.20			
P-D4-5d-HWCS-N	16.47	16.58	4.23	0.32	0.32	14.2	Pull-out
	17.33			0.27			
	15.94			0.36			
P-D4-7d-HWCS-N	15.42	14.91	3.64	0.36	0.36	5.89	Pull-out
	14.96			0.33			
	14.34			0.37			
P-D5-5d-HWCS-N	14.97	14.91	1.41	0.57	0.53	9.74	Pull-out
	14.68			0.54			
	15.10			0.47			
P-D4-5d-HW-N	8.66	9.08	4.42	0.52	0.47	10.65	Pull-out
	9.11			0.43			
	9.46			0.44			
P-D4-5d-FS-N	10.00	9.87	2.40	0.26	0.18	23.81	Pull-out
	10.00			0.21			
	9.59			0.16			
P-D4-5d-CS-N	13.69	13.98	2.36	0.54	0.46	17.56	Pull-out
	13.92			0.38			
	14.34			0.45			
P-D4-5d-N	7.54	7.33	3.24	0.27	0.36	21.70	Pull-out
	7.07			0.41			
	7.36			0.40			
P-D5-5d-HWCS-H	25.06	24.89	0.71	0.36	0.31	14.39	Pull-out
	24.92			0.31			
	24.71			0.27			

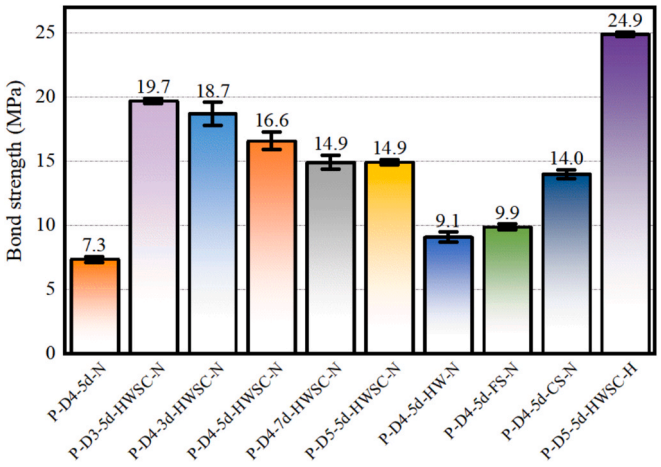


Fig. 14. Bond strength between 3DP-FRP bars and concrete.

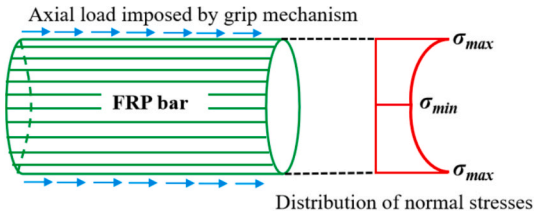


Fig. 15. Shear lag phenomenon.

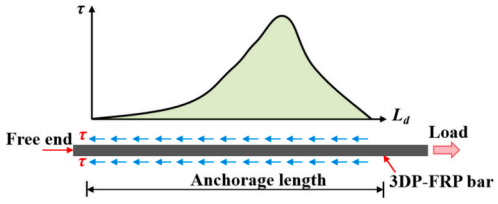


Fig. 16. Distribution of interface bond stress.

demonstrates that the HWCS 3DP-FRP bar displays wave-shaped curves in the residual stage. This behavior results from its superior external bond performance and the sustained frictional interaction between the internal bar's serrated cross-section and concrete, persisting even after the external ribs and sand-coating wore away (Fig. 12(b)). Unlike the findings of this study, previous studies [18,37] demonstrate that conventional helically wrapped and sand-coated (HWSC)-FRP bars exhibit a decreasing trend in residual bond strength. This behavior is attributed to the loss of effective frictional interaction after wear of both the sand-coated surface and ribs, which exposed the smooth inner surface to concrete (Fig. 12(c)).

3.3. Influencing factors

3.3.1. Effect of bar diameter

Fig. 13(a) and Fig. 14 show the relationship between bond behavior and 3DP-FRP bar diameter. For HWCS 3DP-FRP bars with identical surface treatment and an anchorage length equivalent to five times the effective bar diameter, bond strength progressively decreases as bar diameter increases. As the bar diameter increases from 3 to 4, and 5 mm, the bond strength is reduced from 19.69 MPa to 16.58 MPa, and 14.91 MPa, corresponding to reductions of 15.80% and 24.28%, respectively. These findings are consistent with previous studies [53–55]. The main reasons for this can be attributed to the following three aspects: (1) as the diameter of the bars increases, the deformation due to the Poisson effect becomes more pronounced, thereby reducing interfacial friction and mechanical interlock; (2) increased contact area in FRP bars with larger diameters leads to nonuniform stress distribution and diminished effective bond strength; (3) Since the interlaminar shear stiffness of 3DP-FRP bars is lower than that of conventional bars [11,56], differential movements tend to develop between the surface and the core of the 3DP-FRP bars. As a result, the normal stresses in the cross-section are not uniformly distributed, and the surface normal stresses are higher than the core normal stresses, which is known as the "shear lag" effect [54] shown in Fig. 15.

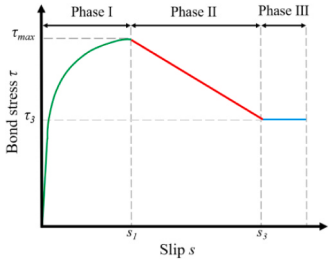
3.3.2. Effect of the anchorage length

Fig. 13(b) shows the curves of the influence of anchorage length on the 3DP-FRP bar concrete bond performance. As shown in the curves, the peak slip increases with anchorage length, while specimens with shorter anchorage exhibit a steeper initial slope in the first stage. It can be seen that with the anchorage length increasing, the average bond strength decreases accordingly. As the anchorage length increases from 15.6 mm to 26 mm, and 36.4 mm, the bond strength is reduced from 18.69 MPa to 16.58 MPa, and 14.91 MPa with reductions of 11.29% and 20.22%, respectively. Similar conclusions of bond strength for anchorage length can be drawn in previous studies [43,57]. As described in Fig. 16, the interface bond stresses distribute unevenly in the bonded region [58,59]. The bond stresses are primarily concentrated near the loaded end, while the free end sustains minimal stress, which causes a reduction in average bond stress over longer anchorage lengths [60].

3.3.3. Effect of the concrete strength

Fig. 13(c) presents bond-slip curves for specimens made with C50 and C80 concrete. The results demonstrate that as the concrete

Table 8
Bond stress–slip model for FRP bars in concrete.

Model name	Functional relationship	Graphical expression
mBPE model [61]	$\frac{\tau}{\tau_{max}} = \begin{cases} (s/s_1)^{\alpha}, & s \le s_1 \\ 1-\eta(\frac{s}{s_1}-1), & s_1 < s < s_3 \\ \tau_3/\tau_{max}, & s > s_3 \end{cases}$	

Note: α is the shape parameter of the ascending branch; τ_3 is the residual bond stress; s_1 is the initial slip of peak bond stress; s_3 is the initial slip on the residual bond stress branch; η is the softening coefficient.

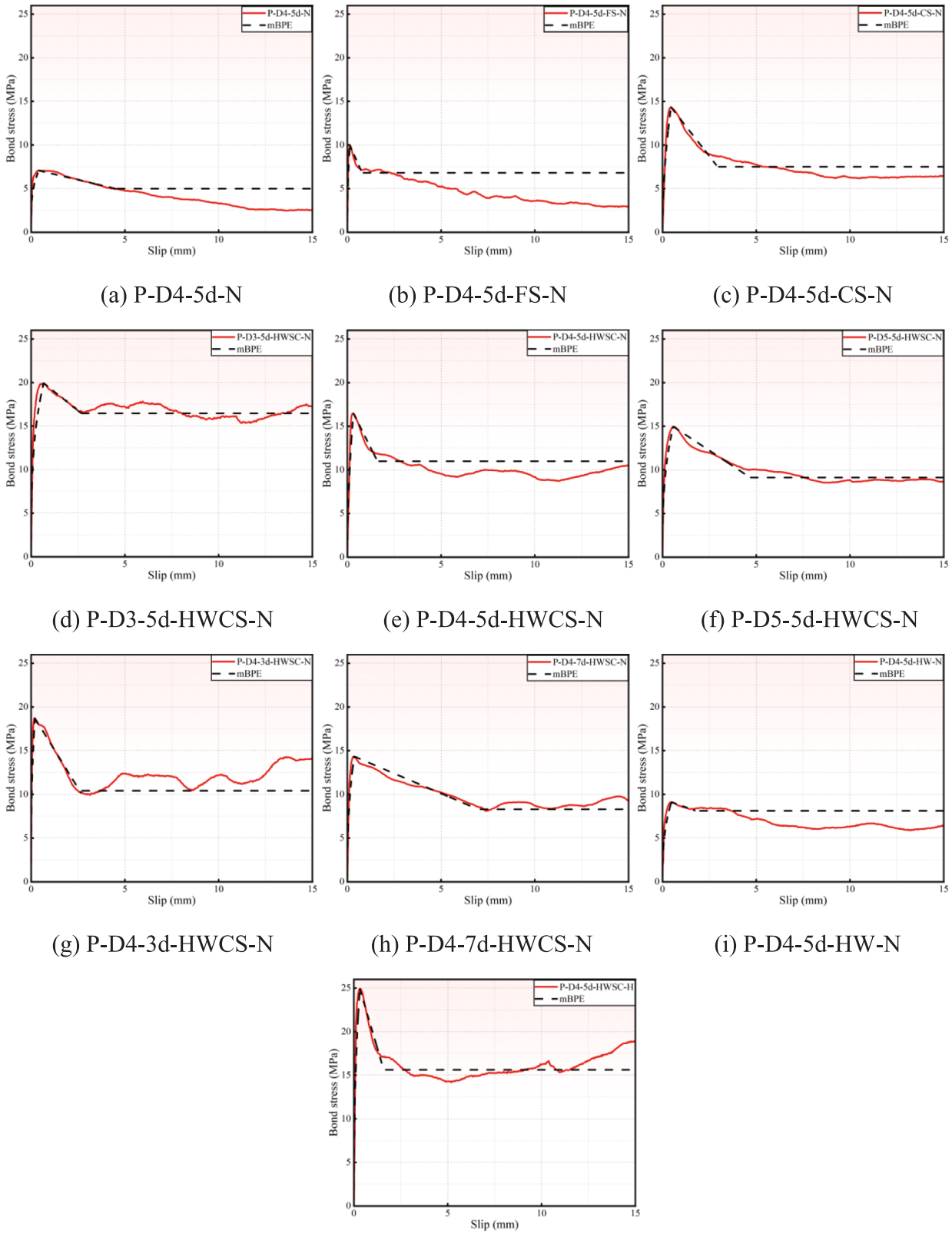


Fig. 17. Comparison between measured and MBPE-fitted bond-slip curves.

Table 9
The fitting parameters of the mBPE model.

Specimen ID	Ascending branch		Decending branch	
	α	R_1^2	η	R_2^2
P-D3-5d-HWCS-N	0.310	0.86	0.057	0.99
P-D4-3d-HWCS-N	0.348	0.87	0.037	0.98
P-D4-5d-HWCS-N	0.524	0.89	0.083	0.92
P-D4-7d-HWCS-N	0.388	0.86	0.023	0.93
P-D5-5d-HWCS-N	0.347	0.92	0.054	0.87
P-D4-5d-HW-N	0.368	0.88	0.039	0.90
P-D4-5d-FS-N	0.458	0.89	0.063	0.82
P-D4-5d-CS-N	0.505	0.90	0.087	0.94
P-D4-5d-N	0.277	0.83	0.030	0.97
P-D5-5d-HWCS-H	0.406	0.84	0.092	0.95

Table 10
Bond strength models for FRP bars in concrete.

Design code or study	Model expression
ACI440.1R-15 [34]	$\frac{\tau_u}{0.083\sqrt{f_c}} = 4.0 + 0.3\frac{c}{d} + 100\frac{d}{l_b}$
CSA-S806-12 [35]	$\tau_b = \frac{d_{cs}\sqrt{f_c}}{1.15(K_1K_2K_3K_4K_5)\pi d_b}$
Yoo et al. [63]	$\frac{\tau_u}{\sqrt{f_c}} = k_1 + k_2\frac{d}{l_b}$
Lee et al. [64]	$\tau_u = 3.3f_c^{0.3}$
Tighiouart. B et al. [65]	$\tau_u = 4.97\frac{\sqrt{f_c}}{d}$
Peng et al. [66]	$\frac{\tau_u}{\sqrt{f_c}} = 1.4 + \frac{3}{d} + 5\frac{d}{l_b}$

Note: c is the concrete cover thickness; d is the FRP bar diameter; l_b is the anchorage length; f_c is the concrete compressive strength; d_{cs} is the the minimum value between (a) the concrete cover thickness of the bar, and (b) two-thirds of the spacing between the centers of the bars (d_{cs} = concrete cover thickness in this study); K_1 is the bar location coefficient; K_2 is the concrete density coefficient; K_3 is the bar size coefficient; K_4 is the bar fiber coefficient; K_5 is the bar surface coefficient; k_1 and k_2 denote the fitting coefficients.

compressive strength increases from 55 MPa to 89 MPa, the bond strength improves from 16.58 MPa to 24.89 MPa with a 49.9% improvement. The experimental results agree with previous studies [33], demonstrating a significant positive correlation between ultimate bond strength and concrete compressive strength. The improved performance results from enhanced chemical adhesion and mechanical interlocking in the high-strength concrete-FRP interface. As shown in Fig. 11(e) and 11(f), at a concrete strength of 55 MPa, 3DP-FRP bars exhibit minor surface damage, while severe surface damage is observed at 89 MPa. No concrete splitting occurs in the above two conditions, which confirms adequate confinement provided by the concrete to the reinforcement. These observations collectively demonstrate a direct correlation between bond performance and the concrete strength.

3.3.4. Effects of 3DP-FRP bar surface condition

Fig. 13(d) compares the bond-slip curves of concrete specimens reinforced with 3DP-FRP bars under different surface treatments. Test results show that untreated smooth pultruded bars display negligible bond strength, which is close to zero and therefore excluded from the figure. By contrast, the untreated 3DP-FRP bars achieve a bond strength of 7.3 MPa. All four surface treatment methods on untreated 3DP-FRP bars significantly enhance the bond strength with varying degrees of improvement. Among them, 3DP-FRP bars with HWCS surface show superior performance with a bond strength of 16.58 MPa, followed by specimens with CS surface at 13.98 MPa. 3DP-FRP bars with FS surface and HW surface show weaker enhancements, achieving bond strengths of 9.87 MPa and 9.08 MPa, respectively. The bond strength of P-D4-5d-CS-N with coarse sand-coated bar reaches 13.98 MPa. This is significantly higher than the 9.87 MPa of P-D4-5d-FS-N with fine sand-coated bar, representing an increase of 42%. The difference is attributed to the surface roughness of the FRP bars. The coarse sand-coated 3DP-FRP bars provide a higher roughness, enhancing mechanical interlocking between the bars and the concrete. The fine sand-coated 3DP-FRP bars exhibit a lower roughness, resulting in a limited bond strength improvement.

The helically wrapped 3DP-FRP bars demonstrate the lowest bond strength enhancement among various surface-treated 3DP-FRP bars. In this study, the 3DP-FRP bars were fabricated by manual winding of PET strands at room temperature, during which the resin did not soften and the surface wrapping relied solely on physical adhesion. In contrast, during the conventional pultrusion process, PET strands are wound at elevated temperatures where the resin softens, thereby significantly enhancing the anchorage between the PET strand ribs and the bar surface. This winding method of 3DP-FRP bars results in superficial physical adhesion of the PET fiber strands to the bar surface, leading to lower bond strength.

The HWCS 3DP-FRP bars demonstrate the highest bond strength among all tested specimens. The surface of the HWCS 3DP-FRP bars combines coarse sand coating and PET strand wrapping. Both the mechanical interlocking from PET ribs and increased surface roughness from coarse sand particles contribute significantly to the enhanced interfacial bond strength.

4. Theoretical analysis

4.1. Analytical model for bond stress-slip relationship

The commonly used FRP-concrete bond-slip models include the CMR model [61], BPE model [62], and mBPE model [61]. The CMR model can only describe the ascending branch of the bond-slip curve but fails to capture the post-peak descending and residual portions. The BPE model has been widely used in existing studies. However, its second-stage horizontal plateau disagrees with the characteristics of the experimental bond-slip curves obtained in this study. Cosenza et al. [61] proposed the modified BPE (mBPE) model shown in Table 8 to improve the bond-slip characterization of the BPE model. The mBPE model demonstrates the closest agreement with the bond-slip curve characteristics observed in this study. The mBPE model is fitted to the bond-slip curves observed in the tests as shown in Fig. 17. The fitting parameters of the mBPE model are shown in Table 9. Comparative analysis reveals that the mBPE model effectively captures both the ascending and descending branches, while providing a more accurate representation of the residual stage.

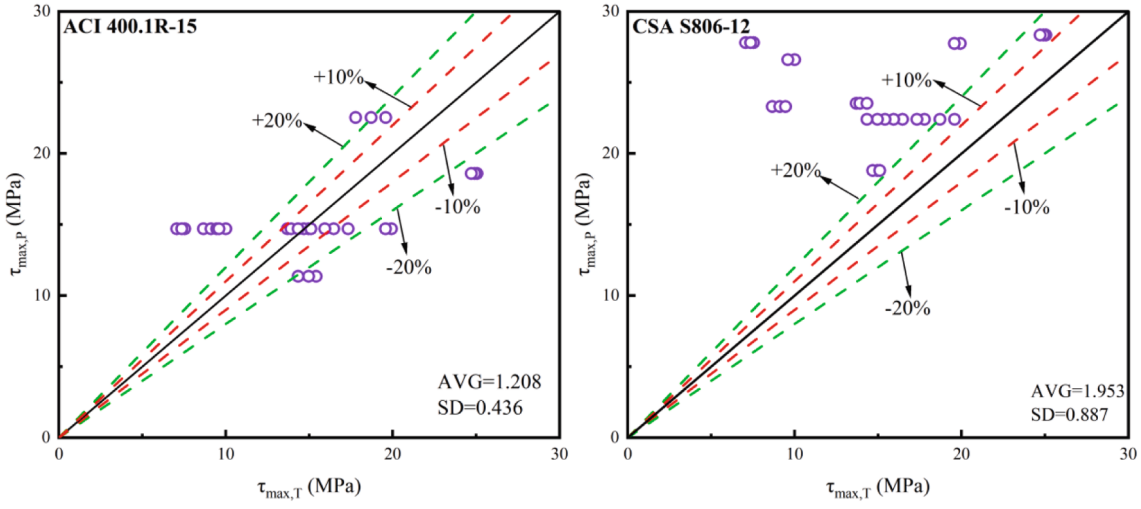
4.2. Prediction models for the bond strength

4.2.1. Existing bond strength models

To date, multiple design codes and research studies have proposed predictive models for conventional FRP bar-to-concrete bond strength. However, the applicability of these models to 3DP-FRP bar-concrete bond behavior remains unverified. Accordingly, Table 10 compares representative models based on their considered parameters. The following statistical parameters are utilized to evaluate the deviations between experimentally predicted bond strength ($\tau_{max,P}$) and measured values ($\tau_{max,T}$). The average performance factor (AVG) is calculated using Eq. (3). The standard deviation of the performance factor (SD) is defined by Eq. (4).

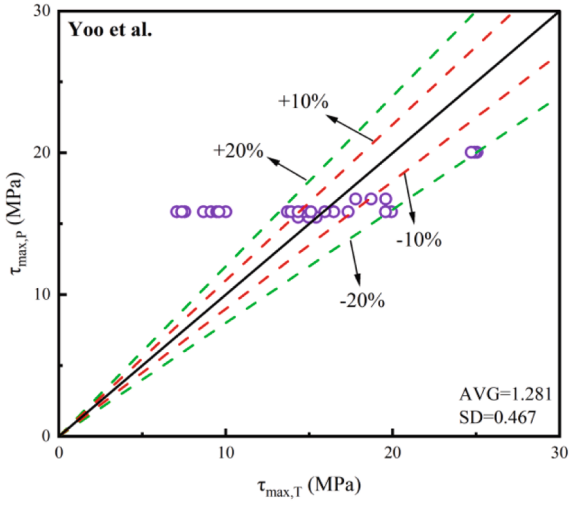
$$AVG = \frac{\sum_{i=1}^{n}\frac{(\tau_{pre})_i}{(\tau_{exp})_i}}{n} \tag{3}$$

$$SD = \sqrt{\frac{\sum_{i=1}^{n}\left[\frac{(\tau_{pre})_i}{(\tau_{exp})_i} - \left(\frac{(\tau_{pre})_i}{(\tau_{exp})_i}\right)_{avg}\right]^2}{n-1}} \tag{4}$$

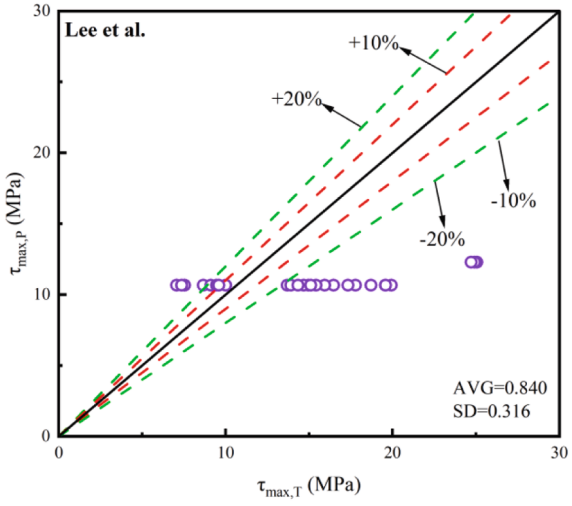


(a) ACI440.1R-15 [34]

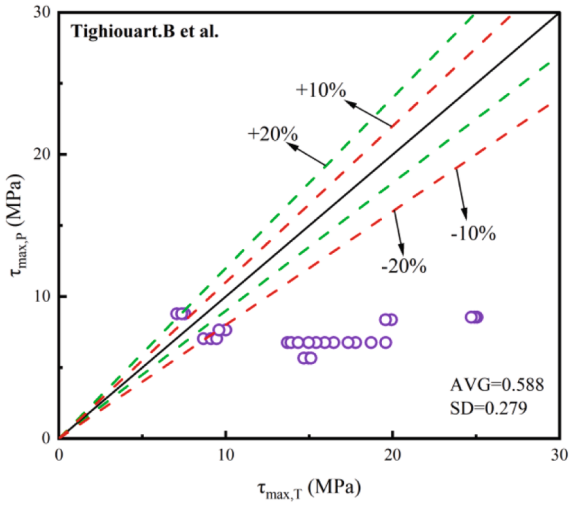
(b) CSA-S806-12 [35]



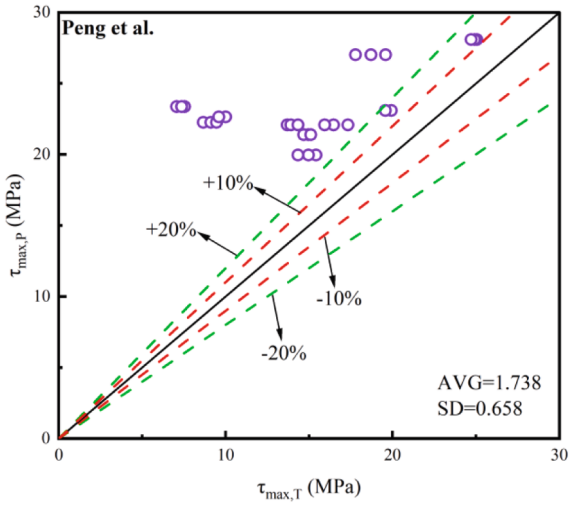
(c) Yoo et al. [63]



(d) Lee et al. [64]



(e) Tighiouart. B et al. [65]



(f) Peng et al. [66]

Fig. 18. Comparisons of test results with predicted bond strength by existing models.

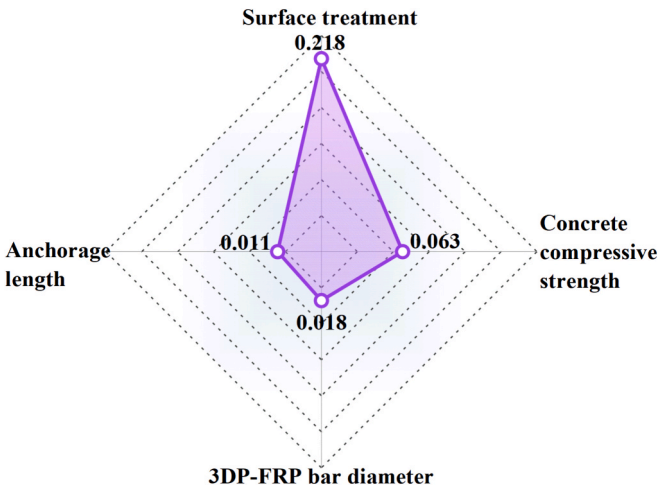


Fig. 19. Normalized variance (σ^2) of bond strength under different influencing factors.

Based on experimental data analysis, as shown in Fig. 18, both the CSA S806-12 model [35] (AVG = 1.953, SD = 0.887) and Peng et al.'s model [66] (AVG = 1.740, SD = 0.824) overestimate the actual bond strength. In contrast, the models by Lee et al. [64] (AVG = 0.840, SD = 0.316) and Tighiouart et al. [65] (AVG = 0.588, SD = 0.279) underestimate the experimental values. The ACI 440.1R-15 [34] (AVG = 1.208, SD = 0.436) and Yoo et al. [63] (AVG = 1.281, SD = 0.467) models showe better accuracy but still exceeded the ± 20% acceptable error range. The ACI 440.1R-15 model [34] incorporates four key parameters: bar diameter, concrete cover thickness, bond anchorage, and compressive strength of concrete. Comparative analysis demonstrates that the ACI 440.1R-15 model [34] with four parameters provides more accurate predictions than Yoo et al.'s model [63] with three parameters.

4.2.2. *Proposed bond strength model*

To systematically evaluate the effects of anchorage length, bar diameter, concrete compressive strength, and surface treatment method on bond strength, this study employs the normalized variance (σ^2) as an assessment metric. The normalized variance is calculated using Equations (5)-(7). In Eq. (5), X_n denotes the normalized bond stress, obtained by dividing the measured bond stress τ_n by the minimum bond stress τ_{min} within the corresponding group. As shown in Fig. 19, the normalized variance coefficients of factors influencing bond strength are as follows: 0.011 for anchorage length, 0.018 for bar diameter, 0.063 for concrete compressive strength, and 0.218 for surface treatment method. Notably, surface treatment exhibits the highest normalized variance coefficient; thus, the surface roughness coefficient should be incorporated as a key parameter in bond strength prediction models.

$$X_n = \frac{\tau_n}{\tau_{min}} \tag{5}$$

$$\overline{X} = \frac{X_1 + X_2 + \cdots + X_n}{n} \tag{6}$$

$$\sigma^2 = \frac{(X_1-\overline{X})^2 + (X_1-\overline{X})^2 + \cdots + (X_n-\overline{X})^2}{n} \tag{7}$$

In this study, the surface roughness coefficient is defined by Eq. (8). Table 11 presents the parameters involved in determining the roughness coefficients for different surface treatments. The specimen ID denotes the surface treatment and bar diameter. For instance, "P-D4″ refers to a 3D-printed FRP bar with an untreated surface, and "HW-D4″ indicates a helically wrapped bar with a nominal diameter of 4 mm.

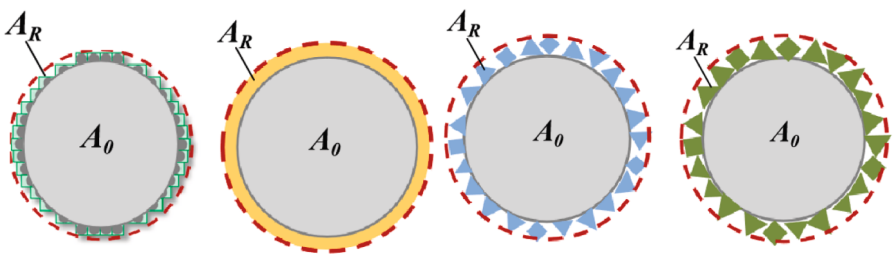
$$\lambda = \alpha \times \lambda_0 = 0.9 \times \frac{\Delta_n}{\Delta_P} \tag{8}$$

where λ_0 is the initial surface roughness coefficient, and λ is the actual surface roughness coefficient. The parameter α represents the reduction factor accounting for manufacturing variations in surface treatment process, particularly those arising from manual rib winding or sand-coating processes. The 0.9 reduction factor is selected to balance structural safety with material efficiency, as lower factors (e.g., 0.7–0.8) would underestimate bond capacity and lead to inefficient material use. Δ_n is the roughness increment of treated bars (i.e., HW-D4, FS-D4, CS-D4), and Δ_P is the roughness increment of untreated bars (i.e., P-D4). Specimen P-D4 remains an untreated surface, thus no reduction factor needs to be applied.

The roughness increment (Δ_n) is obtained by dividing the rough area (A_R) by the inner bar area (A_0) as follows:

Table 11
Surface characteristic parameters of 3DP-FRP bars.

Specimen ID	EffectiveDiameter (mm)	A_l(mm^2)	A_0(mm^2)	A_R(mm^2)	Δ_n	λ_0	λ
P-D4	3.97	12.40	10.48	1.92	0.184	1	1
HW-D4	4.44	15.48	12.40	3.08	0.249	1.35	1.22
FS-D4	4.50	15.90	12.40	3.50	0.283	1.54	1.38
CS-D4	4.70	17.34	12.40	4.95	0.400	2.17	1.96
HWCS-D4	5.20	/	/	/	/	/	2.18



(a) P-D4 (b) HW-D4 (c) FS-D4 (d) CS-D4

Fig. 20. Cross section of the 3DP-FRP bars.

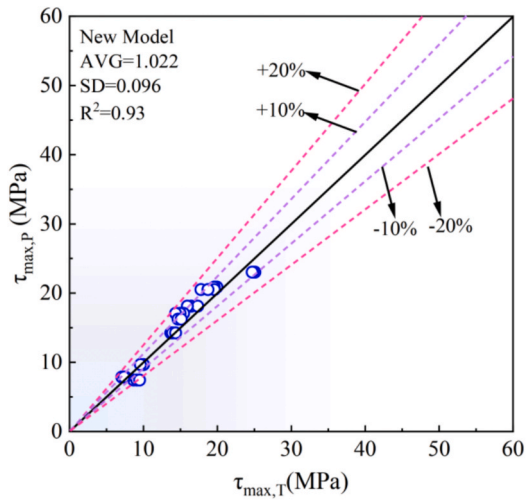


Fig. 21. Comparison of experimental and predicted bond strengths by the proposed model.

$$\Delta_n = \frac{A_R}{A_0} = \frac{A_l\text{-}A_0}{A_0} \tag{9}$$

where A_R is the rough area; A_0 is the inner bar area, and A_l is the cross-section area of 3DP-FRP bar calculated by the effective diameter. For the untreated bars (i.e., P-D4) illustrated in Fig. 20(a), the rough area (A_R) is calculated by subtracting the inner smooth core area (A_0) from the total cross-sectional area (A_l), which represents the total projected area of all serrated surface features. For treated surface bars, such as HW-D4, FS-D4, and CS-D4 in Fig. 20(b–d), A_R is determined by subtracting the bare core area of P-D4 (A_0) from the total cross-sectional area (A_l). In practice, according to ASTM D7205/D7205M-21 [48], the coated and wrapped bars were immersed in water to determine the total volume (V_l), from which the total cross-sectional area ($A_l = V_l / L$) was calculated. The surface treatment was then removed to measure the core volume (V_0) and its corresponding area ($A_0 = V_0 / L$). The cross-sectional area of the treatment layer was determined as $A_R = A_l - A_0$. For the HWCS-D4 specimen, which combined both coarse sand treatment and helical wrapping, the roughness coefficient is calculated by summing the individual roughness coefficients of the coarse sand and helical wrapping treatments, then subtracting the baseline value for P-D4, as expressed by:

$$\lambda_{HWCS} = \lambda_{HW} + \lambda_{CS} - \lambda_P \tag{10}$$

where λ_{HWCS} is the actual surface roughness coefficient of specimen HWCS-D4; λ_{HW} is the actual surface roughness coefficient of specimen HW-D4; λ_{CS} is the actual surface roughness coefficient of specimen CS-D4, and λ_P is the actual surface roughness coefficient of specimen P-D4.

The calculated surface roughness coefficient that accounts for the effects of bar surface treatment is then incorporated into the ACI 440.1R-15 model [34] to develop a new bond strength prediction model for the 3DP-FRP bars. The modified model considers five key parameters, including concrete compressive strength (f_c), cover thickness (c), bond length (l_b), bar diameter (d), and surface roughness coefficient (λ). Through regression analysis, the new bond strength prediction model is established as follows:

$$\frac{\tau_u}{\sqrt{f_c}} = 0.16\frac{c}{d} + 2.43\frac{d}{l_b} + 1.52\lambda\text{-}2.91 \tag{11}$$

Fig. 21 compares the experimental bond strengths with predictions from the proposed model, which achieved high predictive accuracy (R^2 = 0.93). Compared with the ACI 440.1R-15 model (AVG = 1.208, SD = 0.436), the proposed model (AVG = 1.002, SD = 0.096) demonstrates markedly improved prediction accuracy by incorporating the surface roughness coefficient. This improved accuracy provides a theoretical basis for optimizing surface treatment methods for 3DP-FRP bars and for developing more reliable bond strength prediction models.

5. Conclusions

This paper has presented a comprehensive study on the bond behavior between 3DP-FRP bars and concrete, based on 33 pull-out tests and theoretical analysis. The failure modes and corresponding bond-slip curves have been presented and discussed. The interfacial bond properties were analyzed and compared for specimens with different concrete strengths, bar diameters, anchorage lengths, and surface treatment methods. The following conclusions are drawn.

1. The comparative analysis demonstrates that untreated 3DP-FRP bars with serrated surfaces exhibit a higher bond strength of 7.3 MPa compared to pultruded FRP bars with untreated smooth surfaces (approaching zero). This performance advantage highlights the engineering applicability of 3DP-FRP bars, particularly their potential for co-printing with concrete and for off-earth applications where labor is scarce or costly.
2. Four surface treatment methods were evaluated in this study. The bond strengths of the 3DP-FRP bars increased in the following order: untreated < HW (helical wrapping) < FS (fine sandblasting) < CS (coarse sandblasting) < HWCS (helically wrapping and coarse sandblasting). The HWCS was identified as the most effective, exhibiting a bond strength of 16.58 MPa, approximately 2.3 times the value of untreated bars (7.3 MPa), demonstrating a significantly enhanced interfacial performance.
3. A distinctive feature during the residual stage is that 3DP-FRP bars with HWCS treatment and inner serrated cross-sections maintain persistent frictional resistance and exhibit wave-shaped bond-slip curves, providing sustained bond capacity without abrupt failure. These characteristics differ significantly from those of conventional HWSC-FRP bars with smooth inner cross-sections, which experience a decline in bond stress after surface treatment deterioration.
4. The mBPE model demonstrates a satisfactory accuracy in simulating the bond behavior with experimental results, with R^2 values exceeding 0.8 for both the ascending and descending branches of the pull-out test curves, confirming its reliability for 3DP-FRP bars.
5. The surface treatment was quantified through a newly defined surface roughness coefficient, which was subsequently employed in a bond strength prediction model for 3DP-FRP bars. The model demonstrates a good accuracy with an R^2 of 0.93.

This study systematically investigated the bond behavior of 3DP-FRP bars in concrete, developing a predictive model for bond strength based on surface roughness characteristics. The established model provides a theoretical basis for further studies in this field. Future work should focus on evaluating the practical effectiveness of 3DP-FRP bars in structural strengthening applications. Additionally, efforts should promote co-extrusion techniques for the simultaneous printing of FRP and concrete components and off-Earth applications.

CRediT authorship contribution statement

Zi-Tong Yan: Writing – original draft, Software, Investigation. **Xianwen Hu:** Writing – review & editing, Validation, Supervision. **Jie-Kai Zhou:** Writing – review & editing, Supervision. **Yan Zhuge:** Writing – review & editing, Validation, Supervision. **Jun-Jie Zeng:** Writing – review & editing, Writing – original draft, Validation, Supervision, Resources, Project administration, Methodology, Funding acquisition, Formal analysis, Conceptualization.

Declaration of competing interest

The authors declare that they have no known competing financial interests or personal relationships that could have appeared to influence the work reported in this paper.

Acknowledgements

The authors acknowledge the financial support received from the Australian Research Council (FT250100521).

Data availability

Data will be made available on request.

References

[1] Gao S, Sun YJ, Xi L, Zhao T, Huang YX, He RJ, Kang X, Li Y. Recent advances in machine learning-assisted design of additive manufacturing metastructures: a review. Compos. Struct. 2025;372:119525.
[2] Sun HQ, Zeng JJ, Hong GY, Zhuge Y, Liu Y, Zhang YM. 3D-printed functionally graded concrete plates: Concept and bending behavior. Eng. Struct. 2025;327:119551.
[3] Zhang C, Qiao H, Yang L, Ouyang W, He T, Liu B, Chen XY, Wang N, Yan C. Vibration characteristics of additive manufactured IWP-type TPMS lattice structures. Compos. Struct. 2024;327:117642.
[4] Wu J, Li AN, Lyu YH, Yang B, Fu KK, Yang DM. Dual-composite additive manufacturing of glass fiber and recycled carbon fiber reinforced thermoplastic composites with customized fiber layout. Compos. Struct. 2025;354:118815.
[5] Ming YK, Zhang SQ, Han W, Wang B. Investigation on process parameters of 3D printed continuous carbon fiber-reinforced thermosetting epoxy composites. Addit. Manuf. 2020;33:101184.
[6] Wickramasinghe S, Manalo A, Alajarmeh O, Sorbello CD, Weerakoon S, NgoTD Benmokrane B. Advancing polymer composites in civil infrastructure through 3D printing. Autom. Constr. 2025;177:106311.
[7] Almardini AAWH, Yu A, Abbasi S, Ruan D. Enhancing the electrical conductivity of 3D printed continuous carbon fibre reinforced composites via surface coating of MWCNT on filaments. Compos. Commun. 2025;57:102486.
[8] Wang JJ, Li Y, Yu T, Li Q, Li Z. Anisotropic behaviors of moisture absorption and hygroscopic swelling of unidirectional flax fiber reinforced composites. Compos. Struct. 2022;297:115941.
[9] Huang YM, He SJ, Tian XY, Li WD, Mei ZY, Liu P, Kong WY, Lei LM, Wang PZ, Li JJ, Li DC. Multiscale topology optimization and 3D printing of continuous carbon fiber reinforced composites lattice structure. Compos. B: Eng. 2025;304:112691.
[10] Hong Z, Xiong Y, Liang K, Fan CZ, Guo YJ. A strength optimization approach for manufacturable 3D printed variable stiffness laminates with a strain-based approximation. Compos. Struct. 2024;336:117999.
[11] Yan ZT, Zeng JJ, Hu XW, Jiang YY, Zhou JK, Zhuge Yan. Experimental investigation of mechanical properties of 3D-printed fiber-reinforced polymer bars. Structures 2026;84:110877.
[12] Zeng JJ, Jiang YY, Yan ZT, Sun HQ, Huang JH, Zhuge Y. 3D printing of continuous carbon fiber-reinforced polymer reinforcement for concrete columns. Constr. Build. Mater. 2025;502:144415.
[13] Zeng JJ, Yan ZT, Jiang YY, Li PL. 3D printing of FRP grid and bar reinforcement for reinforced concrete plates: development and effectiveness. Compos. Struct. 2024;335:117946.
[14] Zhang MY, Tian XY, Liu TF, Wang PZ, Cao HJ, Li DC. Thermal degradation and performance evolution mechanism of fully recyclable 3D printed continuous fiber self-reinforced composites. Sustain. Mater. Technol. 2023;37:e00706.
[15] Tian XY, Liu TF, Wang QR, Dilmurat A, Li DC, Ziegmann G. Recycling and remanufacturing of 3D printed continuous carbon fiber reinforced PLA composites. J. Clean. Prod. 2017;142:1609–18.
[16] Liao JJ, Zeng JJ, Bai YL, Zhang LH. Bond strength of GFRP bars to high strength and ultra-high strength fiber reinforced seawater sea-sand concrete (SSC). Compos. Struct. 2022;281:115013.
[17] Silva EM, Harries KA, Ludvig P, Sólyom S, Platt S. Experimental investigation of bond and cracking behaviours in GFRP-reinforced concrete members. J. Build. Eng. 2024;83:108434.
[18] Zeng JJ, Sun HQ, Deng RB, Yan ZT, Zhuge Y. Bond performance between FRP bars and 3D-printed high-performance concrete. Structures. 2025;73:108377.
[19] Yoo SJ, Hong SH, Yoo DY, Yonn YS. Flexural bond behavior and development length of ribbed CFRP bars in UHPFRC. Cem. Concr. Compos. 2024;146:105403.
[20] Hu XY, Xue WC, Jiang JF, Yu T, Wang X, Zheng Y, Zeng JJ. Evaluation of splice length of large-diameter GFRP bars in UHPC. J. Build. Eng. 2025;108:112925.
[21] Bakar MBC, Rashid RSM, Amran M, Jaafar MS. Evaluation of the bond-dependent factors for CFRP bars used as structural reinforcement: a critical review. Case Stud. Constr. Mater. 2023;18:e02064.
[22] Zhao X, Rahman MM, D'Antino T, Focacci F, Carloni C. Effect of bonded length on the load response and failure mode of pull-out tests of GFRP bars embedded in concrete. Constr. Build. Mater. 2022;347:128425.
[23] Fan TH, Zeng JJ, Hu XW, Chen JD, Wu PP, Liu HT, Zhuge Y. Flexural fatigue behavior of FRP-reinforced UHPC tubular beams. Eng. Struct. 2025;330:119848.
[24] Zeng JJ, Zeng WB, Ye YY, Liao JJ, Zhuge Y, Fan TH. Flexural behavior of FRP grid reinforced ultra-high-performance concrete composite plates with different types of fibers. Eng. Struct. 2022;272:115020.
[25] Rahman MM, Zhao XD, D'Antino T, Focacci F, Carloni C. Digital image correlation and cracked hinge model applied to notched beams reinforced with GFRP bars. Eng. Fract. Mech. 2024;301:109965.
[26] Zeng JJ, Liao JJ, Zhuge Y, Guo YC, Zhou JK, Huang ZH, Zhang LH. Bond behavior between GFRP bars and seawater sea-sand fiber-reinforced ultra-high strength concrete. Eng. Struct. 2022;254:113787.
[27] Dong HL, Li DF, Yang J. Bond strength prediction model of ribbed FRP bars in concrete. J. Phys.: Conf. Series. IOP Publishing. 2023;2476(1):012018.
[28] Fu L, Zhang LJ, Wang CQ, Wu X, Nakamura H. Numerical investigation on bond behavior between FRP bar and concrete using 3D RBSM with BPE bond-slip model. Structures 2025;75:108806.
[29] Zhang HM, Xiao JC, Ma KJ, Chen J, Liu ZQ, Liu C. Early-age bond behavior of embedded CFRP bars in UHPFRC: test study and theoretical analysis. J. Build. Eng. 2024;86:108862.
[30] Tong DH, Chi Y, Huang L, Zeng YQ, Yu M, Xu LH. Bond performance and physically explicable mathematical model of helically wound GFRP bar embedded in UHPC. J. Build. Eng. 2023;69:106322.
[31] Henin E, Morcous G. Bond behavior of helically wrapped sand coated deformed Glass Fiber-Reinforced Polymer (GFRP) bars in concrete. Constr. Build. Mater. 2021;288:123120.
[32] Wang JZ, Xiao FD, Lai ZY, Yang JL, Tian SY. Bond of FRP bars with different surface characteristics to concrete. Structures. 2024;59:105731.
[33] Lu K, Ai ZC, Feng Z, Chen Z, Yoo DY. Interfacial bond behavior between ribbed CFRP bars and UHPFRC: effects of anchorage length and cover thickness. Eng. Struct. 2023;286:116140.
[34] ACI 440.1R-15. Guide for the Design and Construction of Structural Concrete Reinforced with Fiber-Reinforced Polymer (FRP) Bars. American Concrete Institute, USA; 2015.
[35] Design and Construction of Building Structures with Fiber-Reinforced Polymers . Canada : Canadian Standards Association; 2017.
[36] CSA S6-14. Canadian Highway Bridge Design Code. CSA Group, Canada; 2017.
[37] Solyom S, Balazs GL. Bond of FRP bars with different surface characteristics. Constr. Build. Mater. 2020;264:119839.
[38] Arias JPM, Vazquez A, Escobar MM. Use of sand coating to improve bonding between GFRP bars and concrete. J. Compos. Mater. 2012;46(18):2271–8.
[39] Lai ZY. Study on Bond Performance between FRP Bars with Different Surface Characteristics and Seawater Sea-Sand Concrete under FRP Confinement. M. S. Thesis. Dalian University of Technology. China, 2022. (in Chinese).
[40] He SH, Li LJ, Lin JW, Chen XP, Weng CY, Xiao HS, Liu P, Qiao SH, Xiong Z. Bond performance between ribbed BFRP bar and seawater sea-sand concrete: influences of rib geometry. Structures 2024;65:106660.
[41] Gao JQ. Experimental Study on Bond Performance between FRP Bar with Different Surface Characteristics and Sea-Sand Concrete. M. S. Thesis. Dalian University of Technology. China, 2022. (in Chinese).
[42] Ai ZC. Bond-Slip Behavior between Ribbed CFRP Bars and Ultra-High-Performance Concrete. M. S. Thesis. Guangxi University. China, 2023. (in Chinese).
[43] Liang K, Chen LJ, Shan ZW, Su RKL. Experimental and theoretical study on bond behavior of helically wound FRP bars with different rib geometry embedded in ultra-high-performance concrete. Eng. Struct. 2023;281:115769.
[44] Shan ZW, Liang K, Chen LJ. Bond behavior of helically wound FRP bars with different surface characteristics in fiber-reinforced concrete. J. Build. Eng. 2023;65:105504.
[45] Lin M, Weng CY, Xiao HS, Zeng D, Zhang BF, Chen XP, He SH, Li LJ. Bond performance between fiber-wrapped ribbed basalt fiber-reinforced polymer bars and seawater sea-sand concrete. Buildings. 2023;14(1):38.
[46] Continuous Carbon Fiber (CCF). https://www.anisoprint-cn.com/product-3-2/103.html.
[47] PETG from ESUN. https://www.esunchina.net/petg-product/.
[48] ASTM. D7205/D7205M-21.Standard Test Method for Tensile Properties of Fiber Reinforced Polymer Matrix. USA: ASTM Committe; 2021.
[49] CFRP Bars. https://www.boscfrp.com/product/.
[50] PET Strand. https://eng.maedakosen.jp/.
[51] Sun XY, Gao C, Wang HL. Bond performance between BFRP bars and 3D printed concrete. Constr. Build. Mater. 2021;269:121325.
[52] Caro MC, Jemaa Y, Dirar S, Quinn A. Bond performance of deep embedment FRP bars ep oxy-bonded into concrete. Eng. Struct. 2017;147:448–57.
[53] Baena M, Torres L, Turon A, Barris C. Experimental study of bond behaviour between concrete and FRP bars using a pull-out test. Compos. B: Eng. 2009;40(8):784–97.
[54] Firas SA, Gilles F, Robert LR. Bond between carbon fibre-reinforced polymer (CFRP) bars and ultra high performance fibre reinforced concrete (UHPFRC): Experimental study. Constr. Build. Mater. 2011;25(2):479–85.
[55] El Refai A, Ammar M-A, Masmoudi R. Bond performance of basalt fiber-reinforced polymer bars to concrete. J. Compos. Constr. ASCE. 2015;19(3):04014050.
[56] Lu J. Evaluation of Fundamental Mechanical Properties of Thermoplastic FRP Bars for Concrete Structure. M. S. Thesis. Southeast University. China, 2018. (in Chinese).
[57] Ding T, Qin F, Xiao JZ, Chen XM, Zuo ZB. Experimental study on the bond behavior between steel bars and 3D printed concrete. J. Build. Eng. 2022;49:104105.

[58] Zhou H, Yang Y, Liu K, Huang TL, Ou Y, Zhang SS. Analytical study on the behavior of CFRP-concrete bonded joint with a non-rigid end-anchor. Compos. Struct. 2023; 326:117609.
[59] Li PD, Zhao Y, Wu YF, Lin JP. Effect of defects in adhesive layer on the interfacial bond behaviors of externally bonded CFRP-to-concrete joints. Eng. Struct. 2023; 278:115495.
[60] Achillides Z, Pilakoutas K. Bond Behavior of Fiber Reinforced Polymer Barsunder Direct Pullout Conditions. J. Compos. Constr. ASCE. 2004;8(2):173–81.
[61] Cosenza E, Manfredi G, Realfonzo R. Behavior and Modeling of Bond of FRP Rebars to Concrete. J. Compos. Constr. ASCE 1997;1(2):40–51.
[62] Eligehausen R, Popov EP, Bertero VV. Local Bond Stress-Slip Relationships of Deformed Bars under Genearlized Excititations. Springfield: NTIS; 1983.
[63] Yoo DY, Kwon KY, Park JJ, Yoon YS. Local bond-slip response of GFRP rebar in ultra-high-performance fiber-reinforced concrete. Compos. Struct. 2015;120: 53–64.
[64] Lee JY, Kim TY, Kim TJ, Yi CK, Park JS, You YC, Park YH. Interfacial bond strength of glass fiber reinforced polymer bars in high-strength concrete. Compos. B: Eng. 2008;39(2):258–70.
[65] Tighiouart B, Benmokrane B, Gao D. Investigation of bond in concrete member with fibre reinforced polymer (FRP) bars. Constr. Build. Mater. 1998;12(8): 453–62.
[66] Peng KD, Zeng JJ, Huang BT, Huang JQ, Zhuge Y, Dai JG. Bond performance of FRP bars in plain and fiber-reinforced geopolymer under pull-out loading. J. Build. Eng. 2022;57:104893.